JACS
JOURNAL OF THE AMERICAN CHEMICAL SOCIETY
Article
Cite This: J. Am. Chem. Soc. 2018, 140, 211−218
pubs.acs.org/JACS

Dual-Ratiometric Target-Triggered Fluorescent Probe for Simultaneous Quantitative Visualization of Tumor Microenvironment Protease Activity and pH *in Vivo*

Tiancong Ma,[†,‡] Yi Hou,[†] Jianfeng Zeng,[§] Chunyan Liu,[†] Peisen Zhang,[†] Lihong Jing,[†] Dihua Shangguan,[†] and Mingyuan Gao*[,†,‡,§]

[†]CAS Research/Education Center for Excellence in Molecular Sciences, Institute of Chemistry, Chinese Academy of Sciences, Bei Yi Jie 2, Zhong Guan Cun, Beijing 100190, China

[‡]School of Chemistry and Chemical Engineering, University of Chinese Academy of Sciences, Beijing 100049, China

[§]Center for Molecular Imaging and Nuclear Medicine, School for Radiological and Interdisciplinary Sciences (RAD-X), Soochow University, Collaborative Innovation Centre of Radiation Medicine of Jiangsu Higher Education Institutions, Soochow University, Suzhou 215123, China

Supporting Information

ABSTRACT: The abnormal expression of tumor-associated proteases and lowered extracellular pH are important signatures strongly associated with cancer invasion, progression, and metastasis. However, their malignant effects were mainly identified using cell and tissue studies. To noninvasively visualize the heterogeneous distribution of these abnormal indicators *in vivo* and further disclose their collective behaviors, a target-triggered fluorescent nanoprobe composed of a ratiometric pH-sensitive dye, a near-infrared dye (Cy5.5), and biocompatible Fe_3O_4 nanoparticles was constructed. The pH-sensitive dye was linked through a peptide substrate of matrix metalloprotease-9 (MMP-9) with Fe_3O_4 nanoparticles to establish a Förster resonance energy transfer (FRET) system for sensing the pH of the tumor microenvironment. Cy5.5 served as an internal reference for forming a secondary ratiometric fluorescent system together with the activated pH dye to enable the visualization of protease activities *in vivo*. Extensive imaging studies using a mouse model of human colon cancer revealed that the overexpression of MMP-9 and abnormal microenvironmental pH quantitatively visualized by this dual-ratiometric probe are spatially heterogeneous and synergistically guide the tumor invasion *in vivo*.

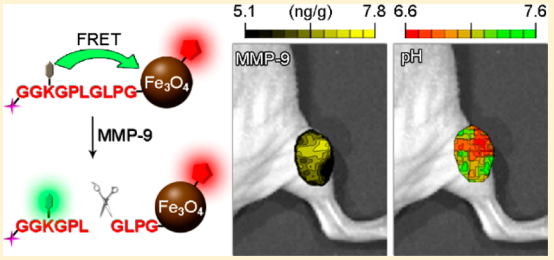

INTRODUCTION

Matrix metalloproteases (MMPs), a family of zinc-dependent secreted endopeptidases, initially drew attention to study an exotic event, the dissolution of the tadpole tail.[1] It was then postulated that MMPs may also promote tumor invasion via enzymatic degradation of basement membrane collagen, which gained support through pathologic studies of tumor transition from in situ to invasive carcinoma.[2] Further cell studies examining the degradation of collagen labeled with ^{14}C revealed that the levels of MMPs secreted by melanoma and sarcoma cells were significantly increased, and in combination with gel electrophoresis, the increased expression of MMPs in tumor explants of skin, colon, lung, ovary, and breast cancer were confirmed and quantified.[3−5] To date, MMPs are known to associate not only with metastasis but also with the regulation of apoptosis, angiogenesis, and the growth of malignant tumors.[6] Unfortunately, the small tissue biopsies typically collected do not necessarily reflect the overall distribution of MMPs in a tumor. Recent studies suggest that it is possible to image the activity of MMPs and other proteases using *in vivo* fluorescence imaging.[7−10] Nanoprobes based on a cyanine dye and a quencher or two self-quenching cyanine molecules covalently linked by an MMP-cleavable peptide have been used to detect protease activity through the cleavage of the peptide linker *in vivo*.[11−13] However, this turn-on type of probes cannot provide quantitative information on MMP expression because it is impossible to separate probe concentration from enzymatic activity.

In addition to abnormal MMP expression, the lowered pH in the tumor microenvironment caused by altered glucose metabolism and enhanced glucose uptake is another important signature of cancer.[14] Low extracellular pH induces cancer cell death, promotes angiogenesis through up-regulating vascular endothelial growth factor expression, and accelerates extracellular matrix degradation by affecting proteolytic enzymes.[15−18] Microelectrode, magnetic resonance (MR) spectroscopy and imaging, and chemical exchange saturation transfer, a new MR imaging technique, have been used for detecting the pH of the tumor microenvironment *in vivo*.[19−21] In comparison with these techniques, fluorescence imaging offers a more convenient and potentially sensitive approach,[22]

Received: August 20, 2017
Published: December 14, 2017

DOI: 10.1021/jacs.7b08900
J. Am. Chem. Soc. 2018, 140, 211−218

Scheme 1. Nanoprobe Injected Intravenously Passes through the Impaired Blood Vessel to Enter Cancerous Tissue[a]

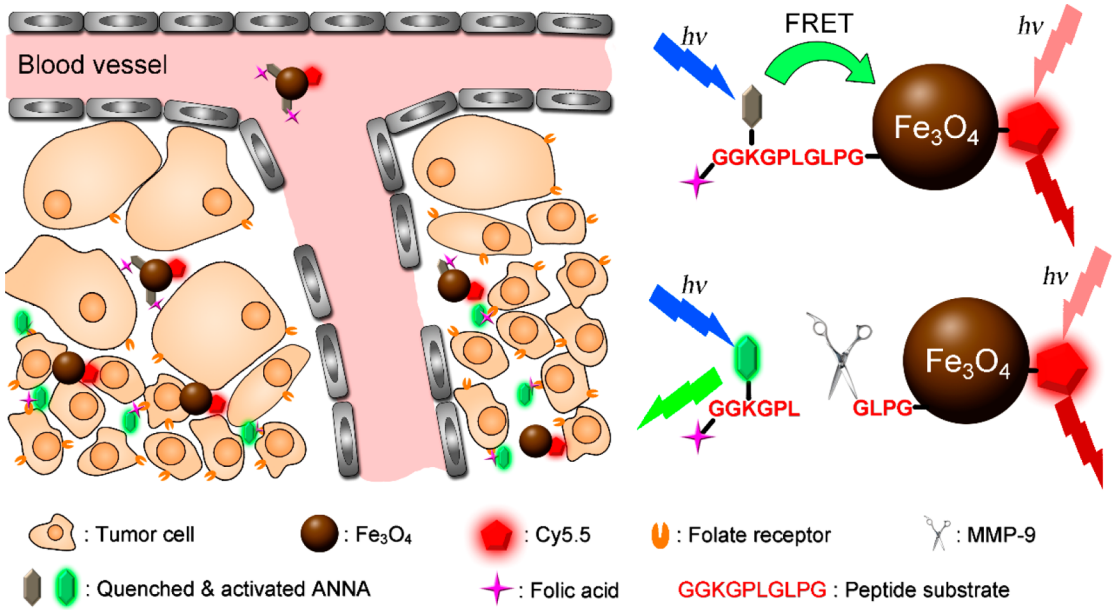

[a]Once within a tumor, the peptide linker connecting ANNA (*N*-carboxyhexyl derivative of 3-amino-1,2,4-triazole fused 1,8-naphthalimide) to an Fe_3O_4 nanoparticle is cleaved by MMP-9 resulting in the activation of the pH sensing fluorophore. By comparing the variable activated emission of ANNA with the constant fluorescence of Cy5.5, MMP-9 activity mapping can be quantified. In this design, Fe_3O_4 particle carrier serves not only as a quencher for ANNA but also as contrast agent for magnetic resonance imaging (MRI) of tumors.

however, the fluorescence intensity of pH-responsive probes can be compromised by a number of other factors. In contrast, ratiometric fluorescent probes can better mitigate these issues and allow quantitative determination of pH,[23−25] yet few ratiometric dyes have been developed for analyzing the microenvironmental pH of tumors *in vivo*.[26,27]

Furthermore, the imaging probes previously reported measure only a single abnormal aspect of the tumor microenvironment, but tumor-associated changes are often multifactorial and strongly correlated.[28,29] To our knowledge, there is no existing literature that quantitatively describes the correlation between MMP activity and the pH of the tumor environment *in vivo*. We present a probe that can serve as a noninvasive tool to map multiple tumor-associated signatures simultaneously in order to determine tumor heterogeneity, correlate abnormal characteristics with metastatic potential, and potentially help predict tumor progression and optimal treatment strategies.

Herein, we design a novel dual-ratiometric fluorescent probe for simultaneously mapping the MMP-9 activity and extracellular pH of tumors *in vivo*. As depicted in Scheme 1, the fluorescence of a ratiometric pH dye ANNA is quenched while attached to the surface of an Fe_3O_4 nanoparticle, representing the "off" state. Upon cleavage of the peptide linker by MMP-9, the fluorescence of ANNA is activated, representing an "on" state, which has been previously demonstrated for *in vivo* pH mapping of tumor xenografts after intratumoral injection.[26] Herein we extend this concept by colabeling our probe with the near-infrared fluorescent dye Cy5.5. Since Cy5.5 is always in an "on" state, the constant Cy5.5 emission and MMP-dependent fluorescence from ANNA can be compared to quantitatively map MMP-9 activity across the entire tumor. In addition, the probe structure was redesigned by replacing the previous tumor-specific monoclonal antibody with folic acid (FA) whose receptor is overexpressed in a large number of malignant tumors.[30,31] Since FA has a much lower molecular weight, the nanoprobe is smaller, which makes it more suitable for systemic delivery. We thus developed a probe that preferentially target the tumor while simultaneously measuring pH and protease activity in a quantitative way.

EXPERIMENTAL SECTION

Experimental details on the preparation of PEGylated Fe_3O_4 nanoparticles with surface reactive maleimide moieties, specific binding assays for dual-ratiometric nanoprobes, animal model construction, fluorescence and MR imaging of tumors *in vivo*, together with histopathological and immunohistochemical assays of tumors harvested, are provided in Supporting Information.

Synthesis of ANNA-Labeled Peptide. ANNA was covalently coupled with the peptide substrate through an amidation reaction between the carboxyl group of ANNA and the side amino group of Lys in the peptide. In brief, 0.84 mg of ANNA was dissolved in 0.2 mL of 0.01 M PBS buffer (pH 8.5), into which 0.2 mL of aqueous solution containing 0.60 mg of 4-(4,6-dimethoxy-1,3,5-triazin-2-yl)-4-methylmorpholinium chloride was introduced. After 5 min, 0.4 mL of aqueous solution containing 2 mg of MMP-9 peptide substrate with the N-terminus protected with Boc was quickly introduced. After reacting for 1 h under stirring, 0.8 mL of trifluoroacetic acid was added to remove the Boc protecting group, which was then removed via rotary evaporation after reacting for one additional hour. The pH of the reaction mixture was then tuned to 6.5 with 5 M NaOH to obtain ANNA-labeled peptide for the following synthesis.

Conjugation of the ANNA-Labeled Peptide with PEGylated Fe_3O_4 Nanocrystals. First, 0.15 mg of 2-iminothiolane hydrochloride was introduced to the solution of ANNA-labeled peptide. After stirring at room temperature for 2 h, 2.5 mL of aqueous solution containing 10 mg of (mal-PEG-dp)-coated Fe_3O_4 nanoparticles was quickly introduced. After 1 h reaction, the resulting conjugates were obtained after purification through ultrafiltration for 4 cycles.

Conjugation of Folic Acid with Peptide-Modified Fe_3O_4 Nanoparticles. Jeffamine derivative of FA was prepared and conjugated to Fe_3O_4 nanoparticles through an amidation reaction

DOI: 10.1021/jacs.7b08900
J. Am. Chem. Soc. 2018, 140, 211−218

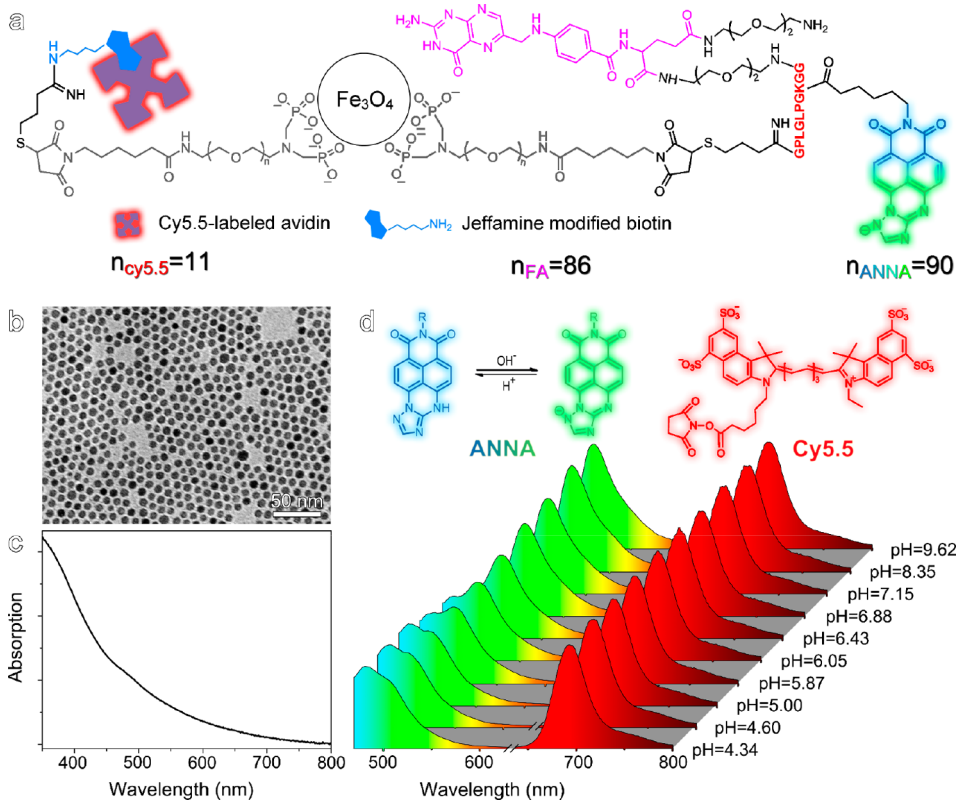

Figure 1. (a) Schematic drawing of structure of the final nanoprobe. (b) TEM image of the Fe_3O_4 nanoparticles. (c) Ultraviolet−visible absorption spectrum of Fe_3O_4 nanoparticles. (d) Protonation-/deprotonation-induced structural transformation of ANNA, chemical structure of Cy5.5, and two sets of fluorescence spectra of ANNA and Cy5.5 recorded at different pH values excited at 455 and 675 nm, respectively.

between the amino group of Jeffamine and the carboxyl residue of the peptide attached on the Fe_3O_4 particle surface. Typically, 1.92 mg of 1-(3-(dimethylamino)propyl)-3-ethylcarbodiimide hydrochloride and 2.88 mg of *N*-hydroxysuccinimide were dissolved in 3 mL of 0.01 M PBS containing 10 mg of Fe_3O_4 particles premodified with ANNA-labeled peptide. After approximately 15 min, 1 mL of 0.01 M PBS containing 1.40 mg of FA-Jeffamine was introduced. Typically, the conjugation reaction was lasted for 10 h. The final conjugates were purified through ultrafiltration and then stored in 1× PBS at 4 °C.

Final Cy5.5 Labeling. Cy5.5 labeling was indirectly achieved through the specific interaction between biotin and Cy5.5-labeled streptavidin. Briefly, 0.75 mg of Jeffamine-modified biotin and 0.30 mg of 2-iminothiolane hydrochloride were first dissolved in deionized water. After stirring for 3 h, another solution containing 10 mg of Fe_3O_4 nanoparticles colabeled with ANNA and FA was introduced. The reaction for biotin labeling via the remaining maleimide groups on the particle surface was allowed to run for 1 h in order to obtain biotin-modified nanoparticles bearing ANNA and FA moieties linked through the peptide substrate of MMP-9.

Cy5.5-labeled streptavidin was prepared as follows: First, 11.75 mg of Cy5.5 was dissolved in 11.75 mL of dimethylformamide and mixed with 2 mL of PBS (0.01 M) containing 3.02 mg of streptavidin. The pH of the reaction mixture was then adjusted to 8.5 with 0.2 M PBS to enable the labeling reaction which was performed for 4 h.

The resulting conjugates were purified through ultrafiltration with 3 kDa MWCO centrifugal filter (Millipore YM-100), then mixed with the biotin-labeled particles obtained above. After approximately 2 h, the dual-ratiometric nanoprobe purified through ultrafiltration was obtained and stored at 4 °C for the following experiments. All animal experiments reported herein were performed according to a protocol approved by Peking University Institutional Animal Care and Use Committee.

RESULTS

Construction of the Dual-Ratiometric Fluorescent Nanoprobe. Hydrophobic Fe_3O_4 nanoparticles of 7.2 ± 0.6 nm were first prepared and PEGylated to obtain biocompatible particles with surface-reactive maleimide moieties.[32−35] Next, as illustrated in Figure 1a, an ANNA-labeled peptide substrate of MMP-9 (i.e., GGKGPLGLPG), was attached to the particle surfaces through click reaction between the particle surface maleimide group and a thiol group stemming from the N-terminus of the peptide. Then, a Jeffamine derivative of FA was linked to the glycine moiety at the C-terminus of the peptide through amidation. Lastly, a Jeffamine derivative of biotin was conjugated to the particle surface through the remaining maleimide groups on the particle surface for further coupling Cy5.5-labeled streptavidin to obtain the dual-ratiometric fluorescent nanoprobe. Through absorption spectroscopy, the number of Cy5.5, ANNA, and FA moieties per Fe_3O_4 particle were estimated to be ca. 11, 90, and 86, respectively. More details are provided in the Supporting Information.

Since the Fe_3O_4 nanoparticles presented in Figure 1b exhibit a broad featureless absorption covering almost the entire visible region (Figure 1c), they are also excellent quenchers for ANNA, as previously demonstrated[26] but not for Cy5.5 because the absorption and emission of Cy5.5 are both in the far near-infrared regions.

Due to the protonation-/deprotonation-induced internal charge transfer, ANNA presents variable emission profiles at different pH as shown in Figure 1d, which makes it possible to optically detect the environmental pH, irrespective of ANNA emission intensity. Most importantly, the integrated ANNA emission is almost independent of pH with only ∼3% of the

DOI: 10.1021/jacs.7b08900
J. Am. Chem. Soc. 2018, 140, 211−218

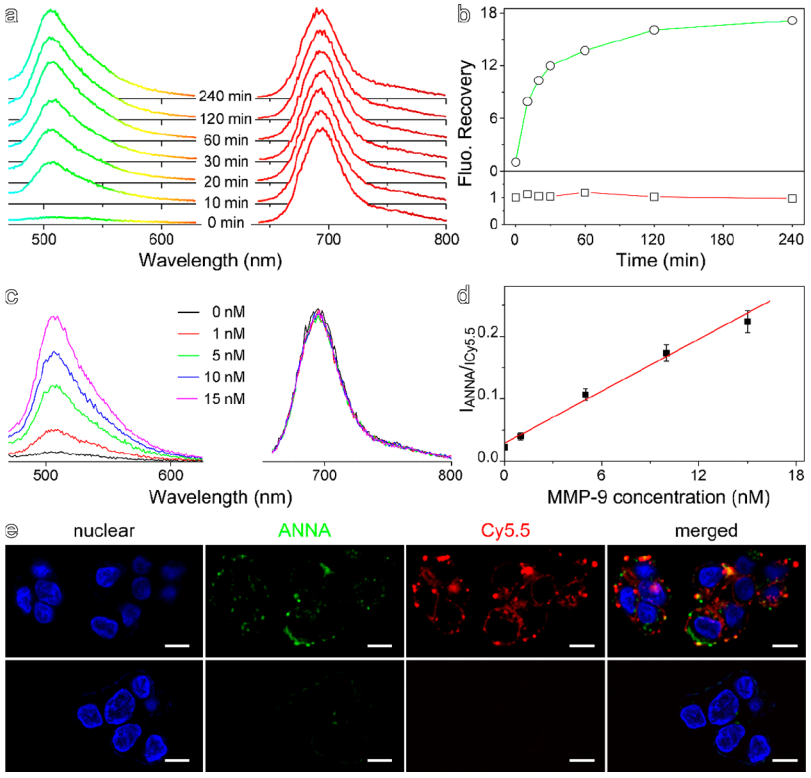

Figure 2. (a) Fluorescence spectra of the nanoprobe recorded upon excitation at 455 and 650 nm, respectively, before (0 min) and after incubation with activated MMP-9 for different periods of time. (b) Temporal evolution of the fluorescence peak intensity of ANNA (green) and Cy-5.5 (red). (c) Fluorescence spectra recorded after the nanoprobes were incubated with different concentrations of activated MMP-9. (d) Linear relationship of integrated emission intensity ratio between ANNA and Cy5.5 ($I_{ANNA}/I_{Cy5.5}$) against the concentration of activated MMP-9 recorded under a fixed incubation time of 30 min. The linear fitting results led to a limit of detection of 0.74 nM with a confidence level of 99.9% for MMP-9 *in vitro*. (e) Confocal microscopy images of LS180 cells (top row) and human fibroblast control cells (bottom row) obtained after incubation with the nanoprobe for 6 h and then imaged through different channels according to the dye emissions (cell nuclei were stained with Hoechst, and the scale bar corresponds to 10 μm).

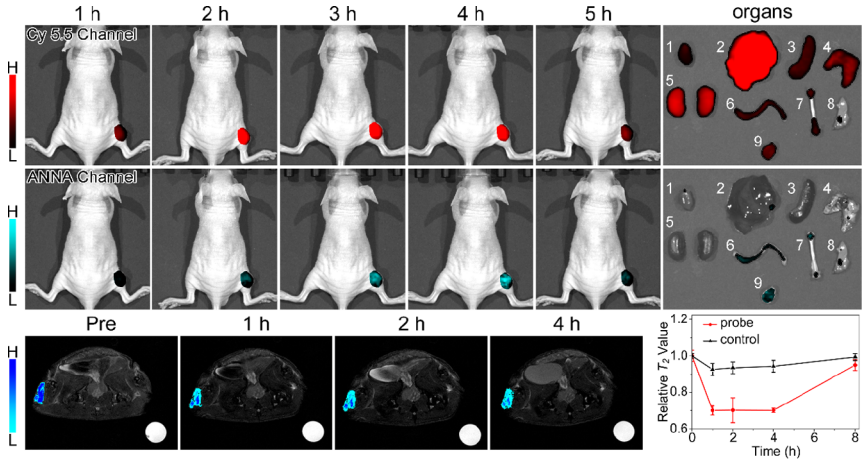

Figure 3. Upper panel: fluorescence images of the tumor site overlaid on the corresponding bright field images of tumor-bearing mice showing the signal variation of both Cy5.5 and ANNA (Right frame 1−9: heart, liver, spleen, lung, kidney, intestine, bone, muscle, and tumor). Lower panel: color-coded T_2-weighted MR images of tumor-bearing mice acquired before and at different time points after intravenous injection of the nanoprobe (Right frame: temporal evolution of T_2 values of the tumor site with a similarly structured nanoprobe bearing no FA as control).

integrated intensity fluctuating in pH range of 5−7 (shown in Figure S1), which enables the following quantification of MMP-9 activity by using the fluorescence of Cy5.5 as an internal reference, as the latter is nearly pH-independent.

Dynamic light scattering (DLS) studies revealed that the hydrodynamic size of the final probes was slightly increased from 21 nm for the PEGylated Fe_3O_4 particles to 24 nm. In addition, as shown in Figure S2, the size distribution profile remained nearly unchanged, suggesting that sequential conjugation reactions took place in a well-controlled manner and that particles did not agglomerate.

Protease-Activated Emission of the Dual-Ratiometric Nanoprobe *in Vitro*. The temporal protease-responsive behavior of the final probe was first evaluated *in vitro* upon

DOI: 10.1021/jacs.7b08900
J. Am. Chem. Soc. 2018, 140, 211−218

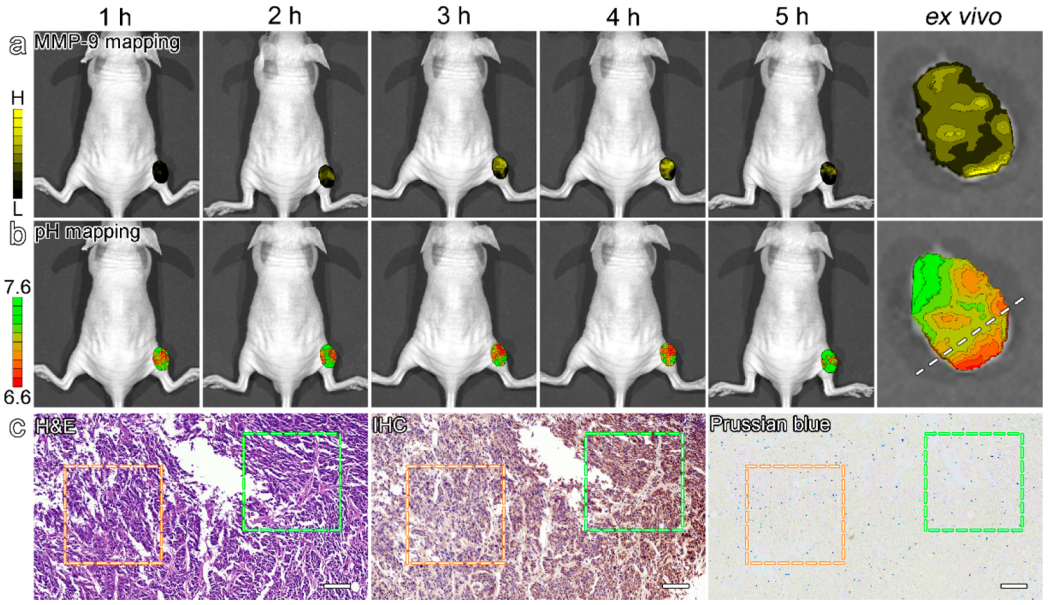

Figure 4. (a, b) *In vivo* contour mapping of MMP-9 activity and pH of the tumor site derived from the results given in Figure 3 (MMP-9 activity derived according to integrated $I_{ANNA}/I_{Cy5.5}$ ratio across the tumor site, and local pH calculated according to pH-dependent ANNA emissions (I_{500}/I_{540}) shown in Figure S5 are quantitatively color-coded with linear scale bars with ten units. With respect to pH, each scale represents 0.1 pH units), together with those of the tumor harvested right after *in vivo* imaging (white dotted line indicates the cross-section of the tumor for tissue analysis). (c) Three adjacent tissue slides stained with H&E, eosin & 3,3'-diaminobenzidine (DAB), and Prussian blue, respectively (scale bar corresponds to 100 μm).

incubation with activated MMP-9 in phosphate-buffered saline (1× PBS, pH 7.4). As shown in Figure 2a,b, the initial fluorescence intensity of ANNA was rather weak but becomes activated upon prolonged incubation with an on/off ratio quickly increasing to 13 within 1 h and approximately 17 within 4 h, while the fluorescence intensity of Cy5.5 remains nearly constant within the same period. In addition, the fluorescence from activated ANNA depends linearly on the concentration of MMP-9 at fixed incubation time, as shown in Figure 2c,d, thus offering a possibility to quantitatively detect MMP-9 using the ratio between ANNA and Cy5.5 emission.

Cancer cell targeting and responsive behavior were investigated by incubating the nanoprobe with LS180, a human colorectal cancer cell line overexpressing MMP-9, or fibroblasts serving as a negative control.[36] The confocal images shown in Figure 2e clearly reveal that the dual-ratiometric probe can target LS180 cells and be activated locally, while control cells do not show any observable fluorescence under the same conditions. In addition, the green emission from the cleaved pH-sensitive dye is also mainly located on the cell membrane. Further quantitative measurements on ANNA emission revealed that the percentage of chromophores remaining attached on the surface of the cell membrane dropped to 76% after incubation with LS180 cells for 2 h. This is probably due to the involvement of lysosomal processes following endocytosis of the probe;[37] however, the non-interlined portion reached a steady state at slightly above 70% after prolonged incubation, which ensures that ANNA fluorescence reflects extracellular pH. More details are provided in Figure S3.

Multimodality Imaging of Tumors *in Vivo*. Multimodality imaging of LS180 tumor xenografts *in vivo* was performed after intravenous delivery of the dual-ratiometric nanoprobe via the tail vein of tumor-bearing mice. As shown in Figure 3, the red fluorescence of Cy5.5 begins to appear at the tumor site 1 h after injection, and the intensity of this red emission continues to increase until it reaches a plateau between 2 and 4 h postinjection before decaying. Alternately, the emission of ANNA appears approximately 2 h post-injection and reaches a signal maximum between 3 and 4 h postinjection. The delay of ANNA reaching its maximum signal can be understood by the cleavage kinetics of MMP-9 shown in Figure 2b. In contrast to the relatively constant spatial intensity of Cy5.5 signal, ANNA intensity is spatially heterogeneous, which was further confirmed by MR imaging as shown in the bottom row of Figure 3. Regarding the inconsistency between the signal patterns of Cy5.5 and ANNA, this could occur because Cy 5.5 signal is strongly associated with the distribution of folate receptor, whereas the ANNA signal is largely governed by the distribution of MMP-9.

Importantly, no signal was evident at the tumor site in control experiments using similarly structured nanoprobes bearing either no FA or mIgG instead of FA, as shown in Figure S4. This demonstrates that the FA moieties endow the dual-ratiometric probe with its tumor targeting ability.[38]

Major organs including the heart, liver, spleen, lung, kidney, intestine, bone, and muscle, as well as the tumor, were excised immediately after the imaging studies and subjected to *ex vivo* fluorescence imaging. The results in the top-right corner of Figure 3 reveal that the nanoprobes are present in most organs and tissues except for muscle. The uptake of nanoprobes by liver, spleen, and bone marrow has been previously observed, as these tissues are rich in phagocytic cells, while the presence of nanoprobes in kidney and intestine suggests that these nanoprobes are eliminated via the renal and biliary clearance pathways.[34] Nanoprobes were also uptaken by the lung, which is similar to what has been previously observed.[39] Although the biodistribution of the nanoprobe is not the central topic of the current study, Cy5.5 can help to indicate the probe's *in vivo*

DOI: 10.1021/jacs.7b08900
J. Am. Chem. Soc. 2018, 140, 211−218

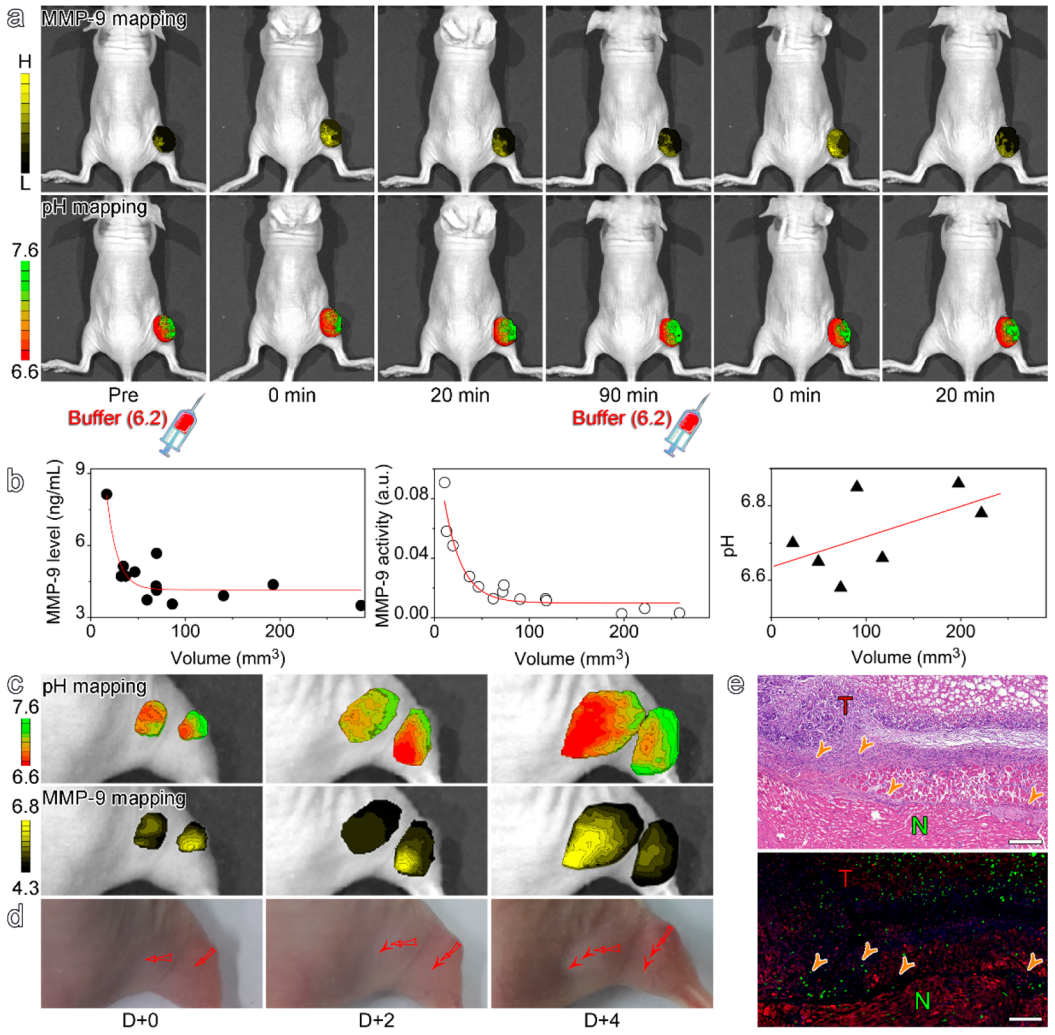

Figure 5. (a) Variation in MMP-9 activity in response to tumor pH adjusted upon intratumoral injection of PBS (pH 6.2). (b) Quantified expression level of MMP-9 obtained through colorimetric assays (left) and relative MMP-9 activity obtained using multimodality imaging (middle), together with tumor microenvironment pH quantified using ANNA emission (right). (c) Quantified pH and MMP-9 expression mapping of tumors obtained at D+0, D+2, and D+4 (in color bar shading from black to yellow for reading MMP-9 expression ranging from of 4.3−6.8 ng/mL, each step thus corresponds to 0.25 units). (d) Photographs of subcutaneous tumors showing their growth over 4 days. (e) Top: microscopic image of a tissue slide stained with H&E; bottom: merged immunofluorescence microscopic image of two adjacent slides stained for E-cadherin expression (red) and MMP-9 expression (green), respectively (scale bar corresponds to 200 μm). The orange arrows point to boundaries between healthy tissue and the tumor where MMP-9 is highly expressed.

biodistribution. In contrast, the ANNA signals are only observed in the intestine, bone, and tumor. Though it remains unclear why intestine and bone present some signal, the signal in these locations is substantially lower than that in the tumor, which suggests that the current dual-ratiometric probe is sufficiently specific for tumor imaging owing to the protease-responsive design.

DISCUSSION

According to our previous studies, pH mapping of tumors can be achieved by quantitatively comparing 500 and 540 nm channel emissions of ANNA upon *in vivo* activation of the ANNA-Fe_3O_4 probe delivered through intratumoral injection.[26] The tissue absorption was taken into consideration for calibrating the I_{500}/I_{540} ratio which was highly sensitive to pH as shown in Figure S5. With improved design, the current probe delivered via the tail vein not only exhibits excellent tumor targeting ability, as demonstrated by the consistency of Cy5.5 signal with ΔT_2 value of the tumor site (Figure 3) but also presents a dramatically increased on−off ratio for ANNA after activation (Figure 2b). Most importantly, the broad time window for Cy5.5 to show constant emission from the tumor site (Figure S6) enables accurate quantification of activated ANNA for mapping MMP-9 activity *in vivo*.

The results shown in Figure 4a suggest that the expression of MMP-9 is spatially heterogeneous but remarkably consistent with the pH mapping given in Figure 4b, especially when ANNA is fully activated 4 h postinjection (Figure S6). This consistency was further verified through *ex vivo* mapping of both MMP-9 activity and the pH of the tumor harvested immediately after *in vivo* imaging experiments, although the signals largely dissipate, as shown in right frames of Figure 4a,b. To understand the uneven distribution of MMP-9 activity, histopathological and immunohistochemical analyses were performed. The results presented in Figure 4c demonstrate that the transplanted tumor cells have formed solid tumors as characterized by large and intensely colored nuclei and irregular sizes and shapes. Although the cells in the

DOI: 10.1021/jacs.7b08900
J. Am. Chem. Soc. 2018, 140, 211−218

green dashed line square are rather similar to those outlined by the orange dashed line upon H&E staining (left panel of Figure 4c), these two regions show different degrees of DAB staining (middle panel of Figure 4c), confirming the heterogeneous distributions of MMP-9 within the tumor. Furthermore, Prussian Blue staining displaying the distribution of the Fe_3O_4-based probe revealed that upon intravenous injection the dual-ratiometric fluorescent probes are almost evenly distributed across the inspected tumor region (right panel of Figure 4b), indicating that MMP-9 mapping using the dual-ratiometric probe appropriately reflects the heterogeneous distribution of MMP-9 *in vivo*.

To further validate the consistency between these two abnormal signatures *in vivo*, the protease activity was mapped while adjusting the tumor microenvironmental pH upon intratumoral injections of 20× PBS buffer (pH 6.2). The results shown in Figure 5a suggest that the activity of MMP-9 is enhanced after the buffer injection but quickly recovered within 20 min, which corresponds well with the pH variations reported by ANNA fluorescence. These phenomena are also reproducible within the same tumor during the second round of pH adjustment after 90 min. Similar experiments carried out via intratumoral injection of 20× PBS buffer (pH 7.4) gave rise to a reverse tendency for the protease activities as shown in Figure S7. The conserved variation of pH and MMP-9 activity thus suggests a strong correlation between these two major abnormal signatures of cancer. To our knowledge, the real-time observation of these two abnormal signatures *in vivo* has not been previously reported. In fact, previous *in vitro* cell experiments, based on gel zymography, Western blot, and reverse transcription PCR, have demonstrated that the expression of MMP-9 can be regulated by altering the environmental pH of cells.[28,40,41] Moreover, the pH-dependent activity of MMPs was also observed through fluorometric assay.[26] In contrast to these time-consuming methods, MMP-9 activities can instantly be observed with the dual-ratiometric probe according to Figure 5a, typically within 10 min, which makes it suitable for real-time acquisition of protease activity for *in vivo* cancer studies.

As a result, it is very important to determine whether secondary dual-ratiometric system established with ANNA/Cy5.5 enables the quantification of protease activity *in vivo* apart from local pH through ANNA. To answer this question, tumor-volume-dependent MMP-9 expression was first determined *ex vivo* through conventional colorimetric assays as seen in the left frame of Figure 5b. Then, the relative protease activity of MMP-9 in tumors of different sizes was determined through *in vivo* imaging with the dual-ratiometric probe for comparison. As shown in the middle frame of Figure 5b, this imaging method offers a profile for tumor-size-dependent MMP-9 activity that is rather similar to the profile obtained using the conventional method except that the sensitivity is slightly lower for larger tumors probably due to the increased light absorption of the tissue in larger tumors. In addition, the ratiometric emissions of ANNA also provide a tumor-size-dependent environmental pH (right frame of Figure 5b) that coincides well with the trend measured using a needle pH microelectrode.[42]

Since the tumor-size-dependent protease activity obtained through imaging is consistent with the tumor-size-dependent MMP-9 activity determined via colorimetric assays (Figure 5b), it is interesting to know whether the imaging signal for MMP-9 activity can further be quantitatively converted to MMP-9 expression level independent of tumor size. The results given in Figure S8 show that integrated imaging signal intensity for MMP-9 activity is linearly related to MMP-9 expression, which enables quantification of fluorescent images for further monitoring of tumor malignancy. This ability may be especially important when assessing the synergistic effects of the overexpressed MMP-9 and lowered tumor environmental pH that are thought to correlate with the invasiveness and metastatic potential of tumors based on *in vitro* studies. By continually monitoring the tumor xenografts for 4 days, the imaging results shown in Figure 5c reveal that the lowered pH regions and high protease activity regions are highly correlated in time and space, pointing to the tumor invasion directions along the development of tumors. This is also supported by the histopathological and immunofluorescence analyses given in Figure 5e, showing that MMP-9 is highly expressed at the boundary between normal and tumorous tissues of the highly invasive site.

CONCLUSIONS

A protease-triggered dual-ratiometric fluorescent probe has successfully been constructed based on a FRET system comprised of Fe_3O_4 nanoparticles, pH-sensitive ratiometric fluorescent dye, NIR dye, MMP-9 specific peptide substrate linker, and FA as a tumor active targeting moiety. In addition to MRI compatibility enabled by Fe_3O_4 portion of the nanoprobe, this rational design allows these intravenously delivered nanoparticles to simultaneously map the protease activity of MMP-9 and microenvironmental pH of tumors. Systematic studies further demonstrate that the dual-ratiometric systems provide not only instant but also quantifiable information on the local protease activity of MMP-9 and pH in tumors. The current study also demonstrated that the overexpression of MMP-9 is well-correlated, in both time and location, with abnormal pH *in vivo*. The synergistic effects of these two characteristics largely govern the heterogeneous invasion of malignant tumors. Therefore, the key novelty of the current study lies in the quantitative and real-time detection of multiple tumor microenvironmental factors through noninvasive multimodality imaging. Thus, we believe that the general concept of the probe design demonstrated herein may represent a powerful tool for studying and characterizing abnormal tumor signatures *in vivo*.

ASSOCIATED CONTENT

Supporting Information

The Supporting Information is available free of charge on the ACS Publications website at DOI: 10.1021/jacs.7b08900.

Preparation of PEGylated Fe_3O_4 nanoparticles with surface reactive maleimide moieties, specific binding assays for dual-ratiometric nanoprobes, animal model construction, fluorescence, and MR imaging of tumors *in vivo*; determination of MMP-9 expression and pH *in vitro* and *in vivo*; pH independency of the integrated ANNA emission; size distribution of the dual-ratiometric probes and the mother PEGylated Fe_3O_4 particles by DLS method; calculation for the percentage of chromophores attached on membrane; color-coded fluorescence images of tumor-bearing mice captured after intravenous injection of the control probes; relationship of microenvironmental pH and I_{500}/I_{540} *in*

DOI: 10.1021/jacs.7b08900
J. Am. Chem. Soc. 2018, 140, 211−218

vivo; temporal evolutions of the integrated fluorescence intensity of Cy5.5 and ANNA at the tumorous region; variation of MMP-9 activities in response to tumor microenironmental pH adjusted (pH 7.4); relationship between the expression level of MMP-9 in tumors of different sizes and $I_{ANNA}/I_{Cy5.5}$ (relative MMP-9 activity) (PDF)

AUTHOR INFORMATION

Corresponding Author

*E-mail: gaomy@iccas.ac.cn. Fax: +86 10 8261 3214.

ORCID

Dihua Shangguan: 0000-0002-5746-803X

Mingyuan Gao: 0000-0002-7360-3684

Author Contributions

T.M., Y.H., and J.Z. contributed equally to this work.

Notes

The authors declare no competing financial interest.

ACKNOWLEDGMENTS

We acknowledge the financial support from NSFC (81671754, 81530057, 81471726, 81571746, 21403250, and 81671755) and CAS (2016YZ01 and PY-2015-32). We thank Dr. Kevin McHugh and Dr. Adam Behrens from MIT for stimulating discussion.

REFERENCES

(1) Gross, J.; Lapiere, C. M. *Proc. Natl. Acad. Sci. U. S. A.* **1962**, *48*, 1014.

(2) Tarin, D. *Int. J. Cancer* **1967**, *2*, 195.

(3) Liotta, L. A.; Tryggvason, K.; Garbisa, S.; Hart, I.; Foltz, C. M.; Shafie, S. *Nature* **1980**, *284*, 67.

(4) Dresden, M. H.; Heilman, S. A.; Schmidt, J. D. *Cancer Res.* **1972**, *32*, 993.

(5) Tarin, D.; Hoyt, B. J.; Evans, D. J.; Ydenberg, R. C. *Br. J. Cancer* **1982**, *46*, 266.

(6) Egeblad, M.; Werb, Z. *Nat. Rev. Cancer* **2002**, *2*, 161.

(7) Withana, N. P.; Ma, X. W.; McGuire, H. M.; Verdoes, M.; van der Linden, W. A.; Ofori, L. O.; Zhang, R. P.; Li, H.; Sanman, L. E.; Wei, K.; Yao, S. B.; Wu, P. L.; Li, F.; Huang, H.; Xu, Z. J.; Wolters, P. J.; Rosen, G. D.; Collard, H. R.; Zhu, Z. H.; Cheng, Z.; Bogyo, M. *Sci. Rep.* **2016**, *6*, 19755.

(8) Ye, D. J.; Shuhendler, A. J.; Cui, L. N.; Tong, L.; Tee, S. S.; Tikhomirov, G.; Felsher, D. W.; Rao, J. H. *Nat. Chem.* **2014**, *6*, 519.

(9) Ai, X. Z.; Ho, C. J. H.; Aw, J.; Attia, A. B. E.; Mu, J.; Wang, Y.; Wang, X. Y.; Wang, Y.; Liu, X. G.; Chen, H. B.; Gao, M. Y.; Chen, X. Y.; Yeow, E. K. L.; Liu, G.; Olivo, M.; Xing, B. G. *Nat. Commun.* **2016**, *7*, 10432.

(10) Yuan, Y.; Wang, F.; Tang, W.; Ding, Z.; Wang, L.; Liang, L.; Zheng, Z.; Zhang, H.; Liang, G. *ACS Nano* **2016**, *10*, 7147.

(11) Lee, S.; Cha, E. J.; Park, K.; Lee, S. Y.; Hong, J. K.; Sun, I. C.; Kim, S. Y.; Choi, K.; Kwon, I. C.; Kim, K.; Ahn, C. H. *Angew. Chem., Int. Ed.* **2008**, *47*, 2804.

(12) Myochin, T.; Hanaoka, K.; Iwaki, S.; Ueno, T.; Komatsu, T.; Terai, T.; Nagano, T.; Urano, Y. *J. Am. Chem. Soc.* **2015**, *137*, 4759.

(13) Weissleder, R.; Tung, C. H.; Mahmood, U.; Bogdanov, A. *Nat. Biotechnol.* **1999**, *17*, 375.

(14) Warburg, O.; Posener, K.; Negelein, E. *Biochem. Z.* **1924**, *152*, 309.

(15) Williams, A. C.; Collard, T. J.; Paraskeva, C. *Oncogene* **1999**, *18*, 3199.

(16) Shi, Q.; Le, X. D.; Wang, B. L.; Abbruzzese, J. L.; Xiong, Q. H.; He, Y. J.; Xie, K. P. *Oncogene* **2001**, *20*, 3751.

(17) Rozhin, J.; Sameni, M.; Ziegler, G.; Sloane, B. F. *Cancer Res.* **1994**, *54*, 6517.

(18) Webb, B. A.; Chimenti, M.; Jacobson, M. P.; Barber, D. L. *Nat. Rev. Cancer* **2011**, *11*, 671.

(19) Volk, T.; Jahde, E.; Fortmeyer, H. P.; Glusenkamp, K. H.; Rajewsky, M. F. *Br. J. Cancer* **1993**, *68*, 492.

(20) Gallagher, F. A.; Kettunen, M. I.; Day, S. E.; Hu, D. E.; Ardenkjaer-Larsen, J. H.; in't Zandt, R.; Jensen, P. R.; Karlsson, M.; Golman, K.; Lerche, M. H.; Brindle, K. M. *Nature* **2008**, *453*, 940.

(21) Chan, K. W. Y.; Liu, G. S.; Song, X. L.; Kim, H.; Yu, T.; Arifin, D. R.; Gilad, A. A.; Hanes, J.; Walczak, P.; van Zijl, P. C. M.; Bulte, J. W. M.; McMahon, M. T. *Nat. Mater.* **2013**, *12*, 268.

(22) Tang, B.; Yu, F.; Li, P.; Tong, L.; Duan, X.; Xie, T.; Wang, X. *J. Am. Chem. Soc.* **2009**, *131*, 3016.

(23) Zhou, J.; Fang, C.; Chang, T.; Liu, X.; Shangguan, D. *J. Mater. Chem. B* **2013**, *1*, 661.

(24) Han, J.; Loudet, A.; Barhoumi, R.; Burghardt, R. C.; Burgess, K. *J. Am. Chem. Soc.* **2009**, *131*, 1642.

(25) Snee, P. T.; Somers, R. C.; Nair, G.; Zimmer, J. P.; Bawendi, M. G.; Nocera, D. G. *J. Am. Chem. Soc.* **2006**, *128*, 13320.

(26) Hou, Y.; Zhou, J.; Gao, Z. Y.; Sun, X. Y.; Liu, C. Y.; Shangguan, D. H.; Yang, W.; Gao, M. Y. *ACS Nano* **2015**, *9*, 3199.

(27) Zheng, X. C.; Mao, H.; Huo, D.; Wu, W.; Liu, B. R.; Jiang, X. Q. *Nat. Biomed. Eng.* **2017**, *1*, 0057.

(28) Rofstad, E. K.; Mathiesen, B.; Kindem, K.; Galappathi, K. *Cancer Res.* **2006**, *66*, 6699.

(29) Johnson, L. L.; Pavlovsky, A. G.; Johnson, A. R.; Janowicz, J. A.; Man, C. F.; Ortwine, D. F.; Purchase, C. F.; White, A. D.; Hupe, D. J. *J. Biol. Chem.* **2000**, *275*, 11026.

(30) Ross, J. F.; Chaudhuri, P. K.; Ratnam, M. *Cancer* **1994**, *73*, 2432.

(31) Bueno, R.; Appasani, K.; Mercer, H.; Lester, S.; Sugarbaker, D. *J. Thorac. Cardiovasc. Surg.* **2001**, *121*, 225.

(32) Park, J.; An, K. J.; Hwang, Y. S.; Park, J. G.; Noh, H. J.; Kim, J. Y.; Park, J. H.; Hwang, N. M.; Hyeon, T. *Nat. Mater.* **2004**, *3*, 891.

(33) Zeng, J. F.; Jing, L. H.; Hou, Y.; Jiao, M. X.; Qiao, R. R.; Jia, Q. J.; Liu, C. Y.; Fang, F.; Lei, H.; Gao, M. Y. *Adv. Mater.* **2014**, *26*, 2694.

(34) Liu, C. Y.; Gao, Z. Y.; Zeng, J. F.; Hou, Y.; Fang, F.; Li, Y. L.; Qiao, R. R.; Shen, L.; Lei, H.; Yang, W. S.; Gao, M. Y. *ACS Nano* **2013**, *7*, 7227.

(35) Qiao, R. R.; Liu, C. H.; Liu, M. H.; Hu, H.; Liu, C. Y.; Hou, Y.; Wu, K. C.; Lin, Y. N.; Liang, J. M.; Gao, M. Y. *ACS Nano* **2015**, *9*, 2120.

(36) Omran, O. M.; Thabet, M. *Ultrastruct. Pathol.* **2012**, *36*, 108.

(37) Lee, G. Y.; Qian, W. P.; Wang, L. Y.; Wang, Y. A.; Staley, C. A.; Satpathy, M.; Nie, S. M.; Mao, H.; Yang, L. L. *ACS Nano* **2013**, *7*, 2078.

(38) Liu, C. Y.; Qi, Y. F.; Qiao, R. R.; Hou, Y.; Chan, K. Y.; Li, Z. Q.; Huang, J. Y.; Jing, L. H.; Du, J.; Gao, M. Y. *Nanoscale* **2016**, *8*, 12579.

(39) Kreyling, W. G.; Abdelmonem, A. M.; Ali, Z.; Alves, F.; Geiser, M.; Haberl, N.; Hartmann, R.; Hirn, S.; de Aberasturi, D. J.; Kantner, K.; Khadem-Saba, G.; Montenegro, J. M.; Rejman, J.; Rojo, T.; de Larramendi, I. R.; Ufartes, R.; Wenk, A.; Parak, W. J. *Nat. Nanotechnol.* **2015**, *10*, 619.

(40) Lee, G. H.; Yan, C.; Shin, S. J.; Hong, S. C.; Ahn, T.; Moon, A.; Park, S. J.; Lee, Y. C.; Yoo, W. H.; Kim, H. T.; Kim, D. S.; Chae, S. W.; Kim, H. R.; Chae, H. J. *Oncogene* **2010**, *29*, 2130.

(41) Kato, Y.; Lambert, C. A.; Colige, A. C.; Mineur, P.; Noel, A.; Frankenne, F.; Foidart, J. M.; Baba, M.; Hata, R.; Miyazaki, K.; Tsukuda, M. *J. Biol. Chem.* **2005**, *280*, 10938.

(42) Engin, K.; Leeper, D. B.; Cater, J. R.; Thistlethwaite, A. J.; Tupchong, L.; Mcfarlane, J. D. *Int. J. Hyperthermia* **1995**, *11*, 211.

DOI: 10.1021/jacs.7b08900
J. Am. Chem. Soc. 2018, 140, 211−218